Proceedings World Geothermal Congress 2020+1
Reykjavik, Iceland, April - October 2021

Microanalysis of Calcite Scaling in a Fractured Geothermal System

David D. McNamara[1], Aaron Lister[2], David J. Prior[2], Aisling Scully[3], Joseph Gardner[1], John Wheeler[1]

[1]Department of Earth, Ocean, and Ecological Sciences, University of Liverpool, United Kingdom

[2]University of Otago, New Zealand

[3]University College Cork, Ireland

d.mcnamara@liverpool.ac.uk

Keywords: calcite, fracture, reservoir, scaling, crystallography, microanalysis, EBSD, EDS, LA-ICPMS, cathodoluminesence

ABSTRACT

The microscopic crystallographic and chemical make-up of geothermal minerals precipitated in fractures within active geothermal reservoirs can record significant information concerning reservoir scaling. It is vitally important to characterize these microscale signatures as they can potentially provide insight into a range of factors that control the onset of fracture scaling and scaling rates, including temperature, pressure, and geothermal fluid composition. By investigating examples of sealed fractures from geothermal systems with a range of microanalytical techniques a deeper understanding of the processes operating during fracture scaling can be obtained. Information on nucleation and growth of scaling minerals in geothermal fractures is crucial in order to incorporate reservoir scaling accurately into reservoir models, and defining fully the influence of secondary permeability in geothermal systems. This study presents results of a multi-staged analysis of calcite scaling in geothermal fracture flow pathways in the Kawerau Geothermal Field, Taupo Volcanic Zone, New Zealand. The application of EBSD, EDS, cathodoluminesce, and LA-ICPMS of calcite sealed fracture samples helps establish the action of 'non-classical' bladed calcite nucleation in the Kawerau Geothermal Field, provides insights into crystal growth processes and growth rates and their controlling conditions such as fluid chemistry and temperature, and provides insights on the effects these processes have on fracture permeability over time.

1. INTRODUCTION

Development of natural and engineered geothermal resources for both electricity generation and direct use is a key target for global renewable energy development (Lu, 2018; Limberger et al., 2018). Fault and fracture networks are crucial components of both natural and engineered geothermal systems in many typical geothermal reservoir rock types including granites, basement terrane metamorphic rocks, and volcaniclastic and sedimentary deposits (McNamara et al., 2017; Genter et al., 1997). In order to function as either an energy or heat resource, fluids need to circulate through a geothermal reservoir to mine subsurface heat, which requires an open fracture network. However, fluid-rock interactions occurring within geothermal fractured systems between the circulating hydrothermal fluids and the mineralogy and morphology of the fracture walls, will result in mineral growth, ultimately resulting in fracture sealing.

Fracture sealing, sometimes referred to as reservoir scaling, is recognized as an important process in geothermal systems (Batzle and Simmons, 1976, Dobson et al., 2003; Genter et al., 2010). Fracture sealing can act in both beneficial and deleterious ways in a geothermal reservoir, such as assisting to hydraulically isolate important subsurface reservoirs, or decreasing fluid migration within a reservoir rock thus negatively impacting the performance and sustainability of the geothermal resource (McNamara et al., 2016; Griffiths et al., 2016). Both calcite and quartz (also present as amorphous silica) are identified as significantly problematic fracture sealing minerals in geothermal systems (Taron and Elsworth, 2009), though other mineral species are also reported as filling fracture flow paths, such as epidote, adularia, zeolites (wairakite, heulandite), clays (kaolinite, illite, smectite), and anhydrite (Hedenquist et al., 1992).

The successful development and longevity of fractured geothermal resources thus relies on maintaining open fracture networks in hot reservoir rocks to allow circulation and extraction of geothermal fluids. A crucial aspect of this must include the development of methods to address the issue of reservoir scaling, which requires the geothermal community to gain a greater understanding of how reservoir fracture scaling occurs. Current research identifies a large range of contributing factors to why and how fracture sealing occurs (not exclusive to geothermal systems) including pressure and temperature conditions of the mineralizing fluid (Sonney and Mountain, 2013), the supply of dissolved material within the mineralizing fluid (Fisher and Brantley, 1992), the mineralogy of the fracture walls (Landrot et al., 2012), the morphology of the fracture walls (Brown, 1995), the physical properties of the precipitating minerals (Urai et al., 1991), and microbial processes (Mountassir et al., 2014). This range of fracture sealing controlling factors has been examined from a number of research perspectives including mechanistic models exploring mineral precipitation on fracture surfaces with grain-scale heterogeneity (Ankit et al., 2015), analogue models of minerals precipitating on fabricated surfaces (Jones and Detwiler, 2016), and direct observation of mineralized fractures using various chemical and crystallographic analytical techniques ranging from standard light microscopy, to scanning electron microscopy techniques (McNamara et al., 2016; Griffiths et al., 2016; Fukuda et al., 2014, Lander and Laubach, 2014, Bons et al., 2012).

This study seeks to further the development of microanalytical methods to explore what the crystallography and chemistry of fracture sealing minerals can tell us about the mechanisms and conditions under which it occurs in geothermal resources. In this paper we present crystallographic and chemical data from geothermal calcite veins causing reservoir scaling in the Kawerau Geothermal Field and analyze this data to provide information on calcite precipitation controls and conditions. This study shows a) deeper analysis of combined electron backscatter diffraction (EBSD) and chemical mapping first explored in McNamara et al. (2016), b) the results from preliminary application of 3D EBSD mapping of geothermal vein structures, and c) quantitative chemical data using in-situ

laser ablation inductively coupled plasma mass spectrometry (LA-ICPMS) to perform U-series dating of calcite, and explore rare earth element (REE) and trace element distributions for information on changes in precipitating fluids over time.

2. MATERIALS AND METHODS

2.1 Geological Setting and Sampling

The Kawerau Geothermal Field is the most northern, active, high temperature (~300 °C), geothermal field in the Taupo Volcanic Zone (Fig. 2), with the resource hosted in Mesozoic greywacke basement composed of medium-grained, andesite–dacite sourced sandstones with minor argillite and chert. Geothermal fluid flow within the Kawerau greywacke basement reservoir is dominated by a series of faults and fractures as evident from NE–SW trending lineaments of hydrothermal features (Christenson, 1987), the spatial relation of structures imaged with borehole image logs to identified zones of permeability (Wallis et al., 2012), and the low permeability of the intact greywacke rock itself (Christenson, 1987; McNamara et al., 2014; Melia et al., 2019). The microanalyses data presented here is acquired from samples of un-oriented, greywacke basement drill-core from well KA30 (Figure 1). Two samples are utilized; a) Sample A: piece of greywacke drill-core (1098-1100 mRF; metres from rig floor) hosting multiple generations of calcite veins, and b) Samples B and C: pieces greywacke basement drill-core (~1213 mRF) hosting calcite veins. Detailed geological and petrographical descriptions of sample A can be found in McNamara et al. (2016), and samples B and C in Lister (2016).

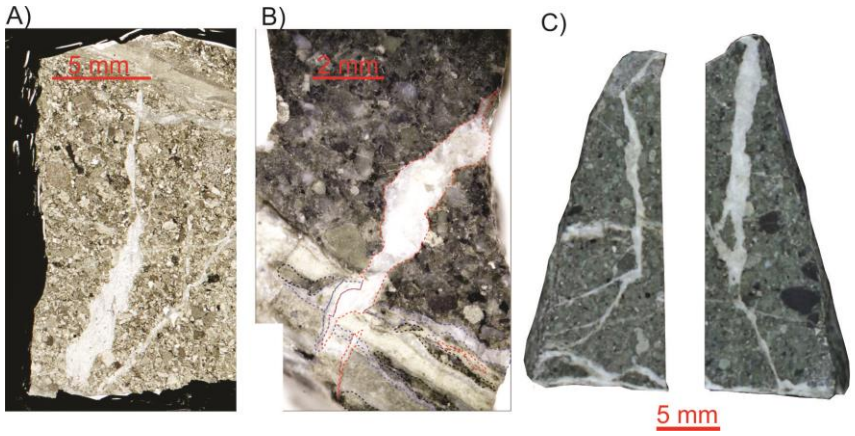

Figure 1: Images of sample material used in this study of calcite ± wairakite veins in greywacke basement core. A) Sample A, B) Sample B, and C) Sample C.

2.2 Microanalytical Procedures

2.2.1 Cathodoluminesence Imaging (CL)

CL imaging is carried out using a Technosyn cold cathode stage mounted on an Olympus BX41 microscope with a trinoc head fitted with a digital camera. The CL apparatus was operated under vacuum (0.05–0.08 Torr / 17–20 V) at an accelerating voltage of 15–20 kV and a beam current of 550–600μA

2.2.2 Energy Dispersive X-Ray Spectroscopy (EDS)

EDX data were collected using Oxford Instruments AZTEC software with a XMAX20 silicon drift detector. Full spectrum EDX data were collected on a grid using an accelerating voltage of 15 to 20 kV and~1–10 nA of beam current. Spectra (including map data) were processed using the TruMap and QCAL procedures within the AZTEC soft-ware. Map data presented here show counts within Kα energy windows corrected for peak overlaps and background counts.

2.2.3 Electron Backscatter Diffraction (EBSD)

All EBSD data is acquired using a Zeiss Sigma variable pressure field emission gun SEM fitted with an Oxford Instruments Nordlys F EBSD camera and an XMax 20 silicon drift EDX detector, at the Otago Centre for Electron Microscopy (OCEM), University of Otago. An acceleration voltage of 30 kV, beam current of ~90 nA, and a working distance of ~20 mm EBSD was used during EBSD acquisition. Both EBSD and EDX data are collected using AZTec software (Oxford Instruments) which undertook initial processing for both techniques. EBSD data is further processed with HKL Channel5 software using methods comparable to Bestmann and Prior (2003). Sample A EBSD was collected using a step size of 2 μm, and 10 μm for Sample C. Characterization of the Burgers vector of dislocations within the calcite crystals and their subgrain walls was carried out using the weighted Burgers vector (WBV) method (Wheeler et al., 2009). This method provides a quantification of the density of geometrically necessary dislocations required to give rise to observed crystal lattice deformation/distortion. It is a weighted method as it preferentially identifies dislocations with lines more steeply inclined to the sample surface, though it does not generate artificial Burgers vectors.

For 3D EBSD mapping, Sample C was first scanned with the Skyscan 1172 μCT Scanner located at the Otago Centre for Electron Microscopy (OCEM). This provided detailed 3-D morphology of the calcite veins in the sample which is then used as guidance for the serial sectioning and EBSD mapping. To attempt to maintain sample integrity during the serial sectioning process, it is encased in a solid briquette of powered KonductoMet, a phenolic mounting carbonite. Following the carbonite mounting process the sample plug was μCT scanned a second time, at a lower resolution, to assess sample integrity and calcite vein orientation in the sample, post mounting process. To maintain constant positioning within the SEM holder and to aid in data analysis the finished carbonite plug included a series of marker schemes. The plug was squared off by machining a flat surface to two edges for a flush fit within the SEM holder, and three 2 mm diameter Fiducial marker holes were drilled perpendicular to the sample surface to assist in orientating the

scanned images in the same x-y orientation during data analysis and image segmentation. Sectioning of the plug was carried out by placing it in a briquette holder for grinding with a weight and a micrometre to monitor the amount removed for each slice. Grinding was preformed using 2100 grit silicon carbide sandpaper until the desired amount of sample was removed, followed by both mechanical and chemical polishing using first 3µm diamond paste and then 1µm diamond paste, with a final polish of colloidal silica to prepare the sample for EBSD. The aim was to achieve surface slices that were 100 µm apart though the separation ranged between 140µm and 700 µm. Seven section surfaces were analyzed in total.

2.2.4 In-situ Laser Ablation Inductively Coupled Plasma Mass Spectrometry (LA-ICPMS)

LA-ICPMS isotopic and geochemical analysis is undertaken at the Otago Community Trust Centre for Trace Element Analysis, University of Otago, using the Resonetics RESOlution M-50-LR excimer (193 nm) laser ablation system. Each investigation site of is pre-ablated to remove contaminates potentially introduced during handling and thin section preparation, before analytical ablation is run. Both laser beam and pre-ablation variables are repeatedly modified during acquisition to find a balance between gaining sufficient chemical data while preventing the laser ablating the underlying glass slide and epoxy in the thin section samples (Table X). LA-ICPMS is performed on the bladed calcite vein from Sample A using both spot and track analyses, and on two bladed calcite veins from Sample B, with three ablation tracks performed on three different sites in each vein (the first track of which is the pre-ablation track). Laser and track parameters for Sample B in-situ testing consist of a laser spot size of Ø 75 µm, a frequency of 10 Hz, and a track speed of 10 μm^{-1} over 40 seconds to produce a track length of 400 µm. For all LA-ICPMS analysis a standard material (Pearce 610J) is used as a reference to eliminate signal drift incurred during data acquisition and correct for erroneous background elemental signatures. Standard signatures were collected three times during laser ablation, once initially before a sample run, secondly between analysis of each sample run, and finally at the conclusion of an ablation run.

3. RESULTS

3.1 Cathodoluminesence Imaging

CL imaging of calcite veins from Sample A to C are shown in Figure 2. Yellow-orange luminescence relates to calcite, and dull blue-white luminescence relates to the geothermal zeolite mineral, wairakite. Calcite luminescence is activated by Mn, Pb, and several rare Earth elements (REEs, e.g. Ce, Eu), and is quenched by Fe, Ni, and Co (Long and Agrell, 1965; Machel, 1985). As such, the more yellow the calcite appears in CL imaging the higher its Mn, Pb, and/or REE content, while more red colors show higher Fe, Ni, and/or Co content in calcite. Samples A and C show a later generation, bladed calcite vein with higher luminescence, offsetting an older, lower luminescent, blocky calcite vein (Figure 2). Bladed calcite in all three samples displays asymmetrical concentric zonation of alternating duller luminescent (Fe/Ni/Co-richer), and brighter luminescent (Mn/Pb/RRE-richer) calcite. Broadly these calcite blades show a brighter crystal core, rimmed by duller calcite with a sawtooth type pattern, rimmed again by brighter calcite (Figure 2). Blocky calcite veins in samples A-C display stronger red CL colors (higher Fe/Ni/Co) giving them a duller appearance than the bladed calcite veins. CL zonation in the blocky calcite is less apparent with no discernible pattern.

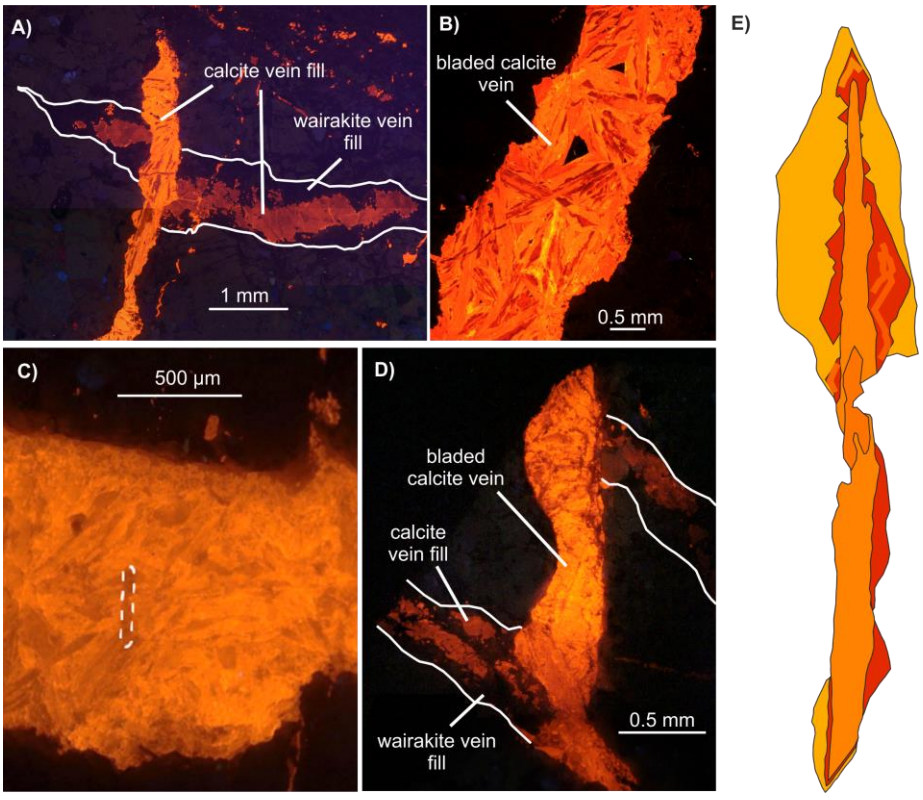

Figure 2: CL images of A) two generations of calcite veining in Sample A. B) Bladed calcite in the later generation calcite vein in Sample A showing zonation in luminescence. C) Zonation patterns in a bladed calcite vein from Sample B (dashed white line indicates damage caused by ablation during LA-ICPMS). D) two generations of veins in Sample C with zoned bladed calcite in the later generation vein. E) Diagram of distinct calcite growth phases of one single calcite blade delineated from CL zonation (from Sample A, bladed calcite vein).

3.2 EDS

EDS mapping of calcite veins in Sample A show a chemical zonation pattern in both the bladed and blocky calcite veins that matches that observed with CL imaging (Figure 3). EDS Fe, Mn, and Ca maps and linescan profiles across the bladed calcite zonation patterns reveal that the duller luminescent zones (more red in color) have higher Fe wt% than brighter luminescent zones (more yellow in color).

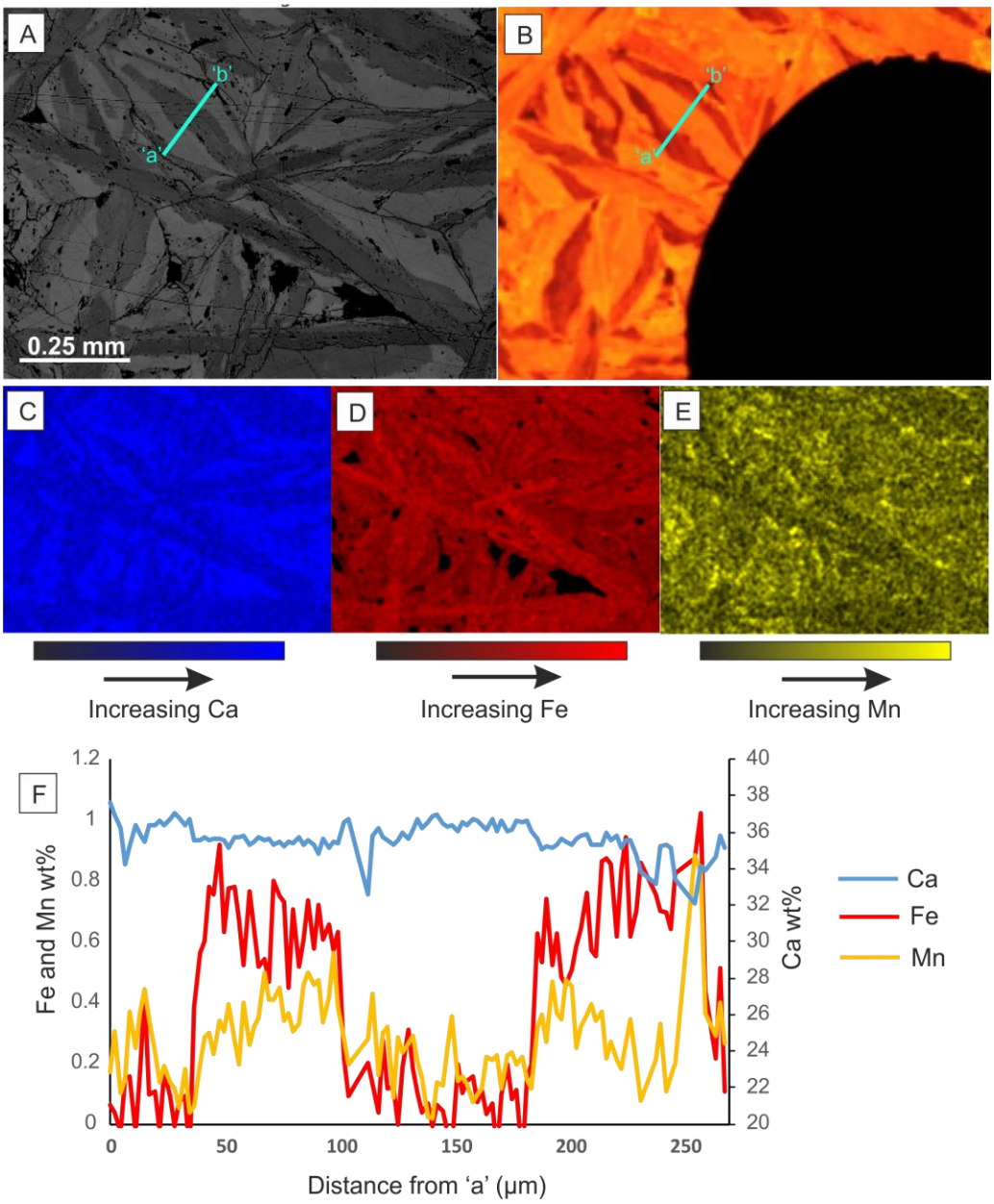

Figure 3: A) Electron image of bladed calcite from Sample A; greyscale variation corresponds to chemical zoning in calcite, 'a' to 'b' is the profile of the EDS linescan. B) CL image of the region shown in (A). C) Calcium count EDS map, D) Iron count EDS map, E) Manganese count EDS map. F) EDS linescan showing variation in Ca, Fe, and Mn wt% across a zoned calcite crystal from 'a' to 'b'.

3.3 EBSD

3.3.1 Bladed Calcite Crystallography

Here we present results from misorientation rotation axes (MRA) and weighted Burgers vector (WBV) analyses for single crystals of bladed calcite and twinned calcite from the two generations of calcite veins from Sample A (Figure 4 and 5). Calcite blades in the younger fracture are elongate perpendicular to the *c* axis. Few contain subgrain boundaries (defined here by crystallographic misorientations of >2°), though texture component maps of single calcite blades reveal crystal distortion of <2° exists along their long axes (as shown in McNamara et al., 2016). Of ten single calcite blades examined the most common MRA for misorientation angles <2° is the <0001> (*c* axis), though some crystals show an MRA on $<11\bar{2}0>$ (*a* direction), an *m* pole, and one crystal with $<02\bar{2}1>$ (*sd* direction). Where visible, subgrains in bladed calcite crystals show MRAs on *m* poles for boundaries with 2°-5° and the *sd* direction for 5°-10° misorientation boundaries. WBV analysis shows that within single bladed calcite crystals the dominant Burgers

vector is some combination of both the *a* direction and the *m* pole where crystals show minimal, if any, substructure, *c* direction Burgers vector for subgrain boundaries with 2°-5° misorientation, and an *f* pole ($01\bar{1}2$) Burgers vector for 5°-10° subgrain boundaries.

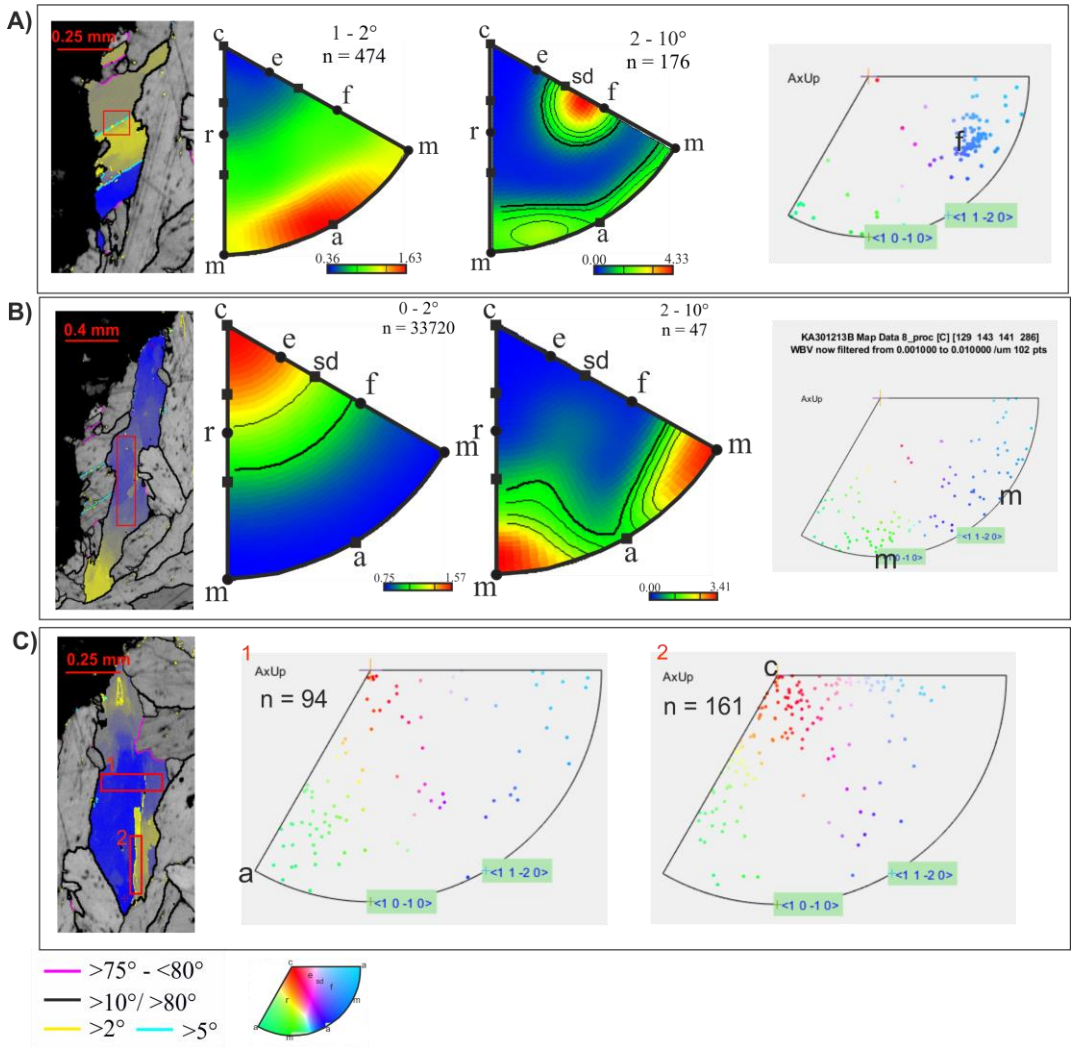

Figure 4: A) Texture component map (blue is 0° misorientation, yellow is 13°) of a single bladed calcite crystal, with contoured inverse pole figures for misorientations within the crystal for 1°-2° and 2°-10° misorientations, and an inverse pole figures of weighted Burgers vectors for the area delineated by the red square. B) Texture component map (blue is 0° misorientation, yellow is 6°) of a single bladed calcite crystal, with inverse pole figure for misorientations within the crystal for 0°-2°, and 2°-10° misorientations, and an inverse pole figure of weighted Burgers vectors for the area delineated by the red square. C) Texture component map (blue is 0° misorientation, yellow is 6°) of a single bladed calcite crystal, and an inverse pole figures of weighted Burgers vectors for the area delineated by the red squares (1 in an area with minimal substructure, 2 across a 2°-5° misorientation subgrain boundary). Texture component maps are overlaid by grain boundary maps color coded to the key at the bottom of the figure. All inverse pole figures for weighted Burgers vectors are colored for the inverse pole figure in the key at the bottom of the figure.

Calcite crystals in the older generation grow across the vein and are heavily twinned (common calcite e-twins). Additionally, they show development of subgrain boundaries (misorientations >2°) and crystal orientation distortion, similar to that observed in the bladed calcite though with no relationship to the calcite crystal shape. From calcite crystals examined from the older fracture, the most common MRA for misorientations <2° is , and for 2°-5° and 5°-10° subgrain boundaries subgrain boundaries it is the *a* direction (Figure 5). WBV analysis shows that distorted regions of calcite crystals have a dominant Burgers vector of *c*, for 2°-5° misorientation subgrain boundaries it is also *c*, and for 5°-10° subgrain boundaries it is a combination of *a* and *m* (Figure 5).

3.3.2 3D-EBSD

Figure 6 shows the results of serial grinding and EBSD mapping of the geothermal calcite vein from Sample C. Individual calcite crystals can be seen to occur in similar locations within the vein as you move down through the sections, evidenced by the same IPF coloring from map to map. The left-hand side of the vein shows a large calcite crystal (ref IPF Z color) that dominates the vein not only from fracture wall to wall in the x-y plane, but also to ~1.5 mm in the z-direction of the vein. Further along the z direction this red calcite crystal shows interlocking textures with other calcite crystals similar to the texture observed for bladed calcite crystals from these samples in McNamara et al. (2016). In the mid-section of the vein (before it bifurcates) the top EBSD map shows a large calcite crystal dominates the vein (orange to pink IPF Z color). Only ~0.5 mm between this section and the one underneath this large crystal texture gives way to vein zone of multiple, smaller calcite crystals that display an interlocking texture. This texture persists

from here to the deepest investigated slice in this vein. In the right-most branch on the right-hand side of the vein similar calcite crystal textures can be seen, large crystals spanning the width of the vein, and appearing to be at least 0.5-1.5 mm in length in the z-direction of the vein (e.g. the calcite crystal colored bright blue).

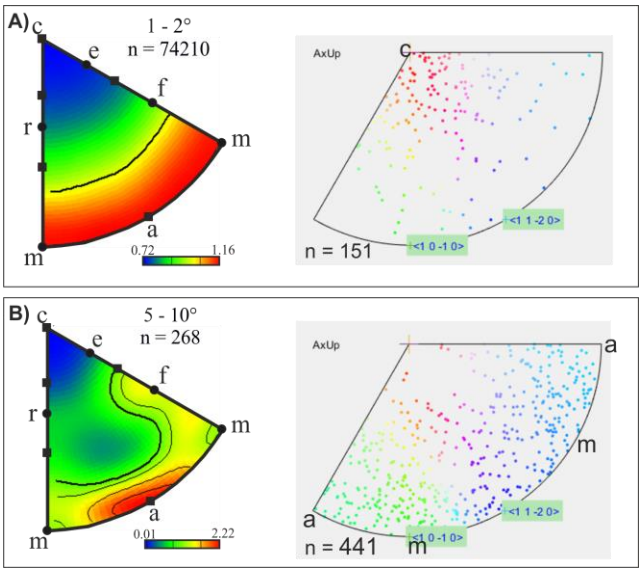

Figure 5: A) MRA (left) and WBV (right) inverse pole figures for regions of calcite with <2° distortion. B) MRA (left) and WBV (right) inverse pole figures for 5°-10° subgrain boundaries in calcite crystals in the older fracture.

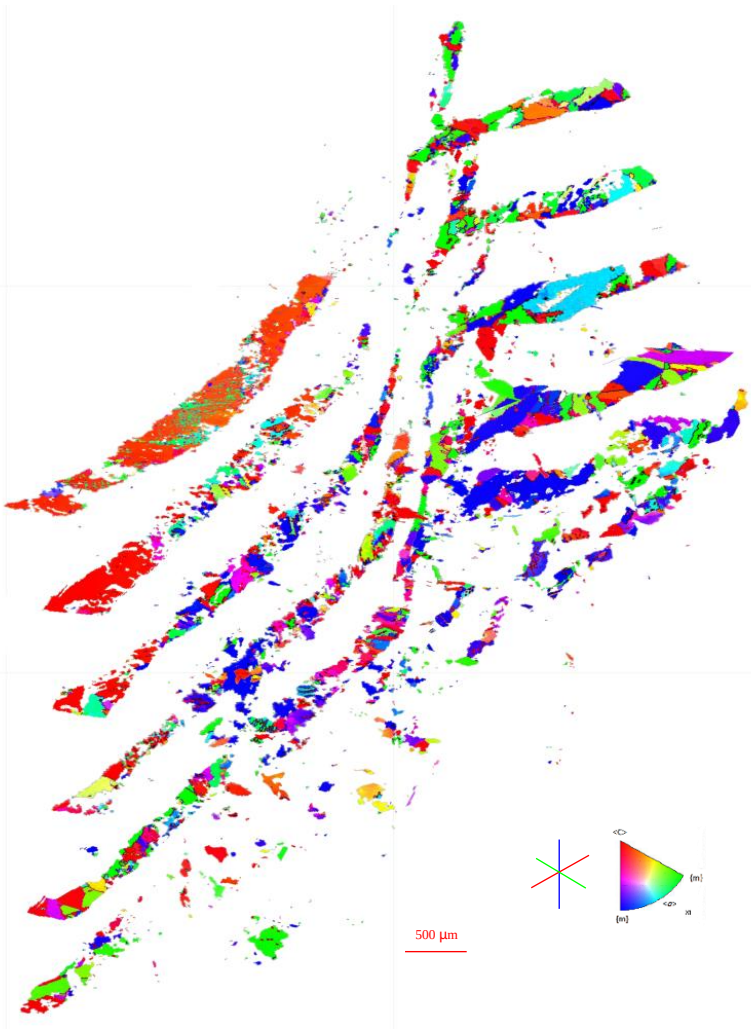

Figure 6: 3-D image stack of the seven EBSD maps of the geothermal calcite vein from Sample C. Calcite crystals are colored for inverse pole figure coloring in the Z direction.

3.4 LA-ICPMS

U and Th concentrations in bladed calcite in Sample A, across a range of luminescent zones, ranges from 0.003-0.3 ppm and 0.01-0.61 ppm respectively (Figure 7). In Samples B and C, bladed calcite U concentrations range from 0.013-0.05 ppm and Th concentrations range from 0.08-0.30 ppm (Figure 7). No correlation is evident between U or Th content and CL zonation, location within a calcite crystal, or location within the crystal (core or rim).

Chondrite normalized REE plots are shown in Figure 8 for all LA-ICPMS spots measured in all bladed calcite veins investigated. Data shows a light REE enriched pattern (negative slope) for bladed calcite from all three samples. Bladed calcite crystals show both positive and negative Eu anomalies, though negative Eu anomalies are only noted in calcite crystals or zones of a calcite crystal with duller luminescence (more red in CL images). Both negative and positive anomalies are noted in bladed calcite in Sample A and B, however Sample C vein calcite only records a positive Eu anomaly.

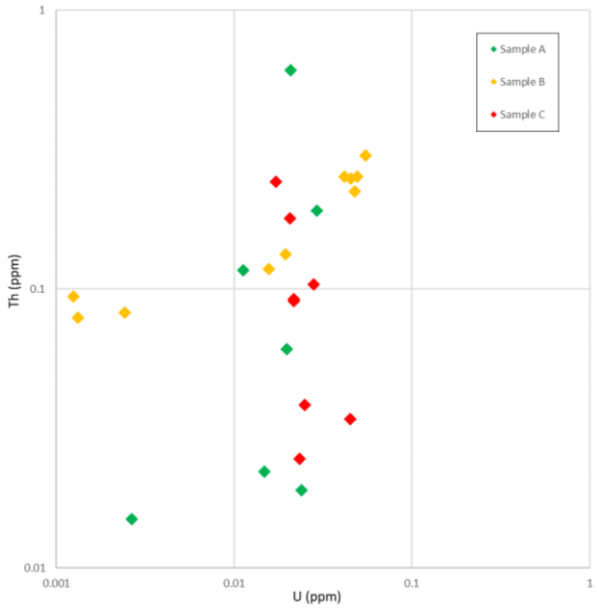

Figure 7: Graph of U against Th (ppm) concentrations within calcite blades from Sample A-C.

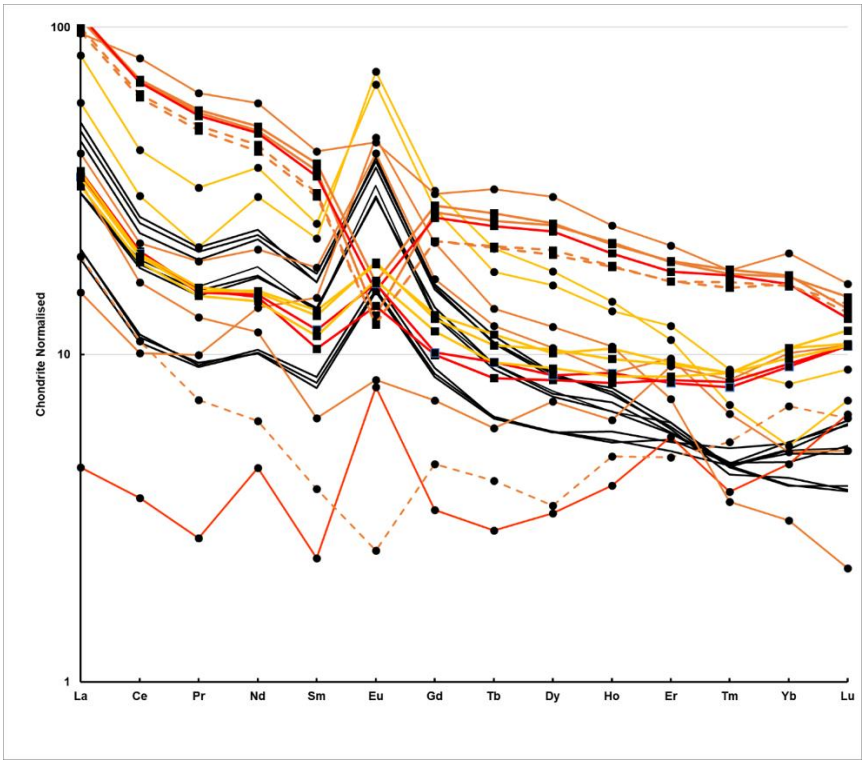

Figure 8: Chrondrite normalized REE plot of LA-ICPMS data on geothermal bladed calcite. Lines are colored based on CL zonation (the more red the color the higher the Fe concentrationin calcite, the more yellow the lower the Fe concentration), and black lines are data where the CL zonation is unknown. Lines with circles represent calcite REE data from Sample A, lines with squares are from Sample B, and the black lines are from Sample C.

4. DISCUSSION

4.1 Insights into calcite reservoir scaling nucleation and growth

Examination of CL patterns show a staged growth for bladed calcite in fluid flow fractures in the Kawerau Geothermal Field, evidenced by temporal breaks in calcite precipitation identified by sharp calcite chemistry zonation boundaries. Initial growth of relatively low-Fe calcite occurs quickly perpendicular to the c-axis establishing a skeletal scaffold of calcite blades within the fracture itself. This scaffold likely serves to maintain a level of permeability within the fracture, propping it open. Subsequent precipitation of relatively high-Fe calcite then occurs on this existing scaffold. This precipitation occurs topotactically as there is no systematic crystallographic orientation change across chemical zones within a calcite blade. This stage of calcite growth can be presumed to be slow, at least in comparison to other stages, as it forms only a thin calcite zone on the blades and calcite growth is inhibited when incorporating more iron (Meyer, 1984; Katz et al., 1993). This would suggest that the permeability of these fractures was able to be sustained for a period of time after the initial precipitation of calcite in response to pressure induced boiling conditions. This would require initial calcite blade growth to be fast, in order to bridge and prop open the fracture to maintain aperture, which may be possible as it has been observed by Tulloch (1982) who noted that bladed calcite can grow perpendicular to the c-axis at a rate of ~0.1mm/day. Following this period of slow, relatively Fe-rich calcite, the remaining open space within the fracture is closed up by the precipitation of calcite with relatively low-Fe content, likely occurring at a faster rate, completely sealing the structure closed.

As reported in McNamara et al. (2016), geothermal bladed calcite examined from the Kawerau Geothermal field has a preferential growth direction perpendicular to the c axis. This is termed length-slow calcite, meaning the c axis is perpendicular to the calcite crystal length. It had been thought that length-slow calcite forms through mineral replacement, as open-space calcite growth was predominantly observed to be length-fast (c axis parallel to the crystal long axis), though it has since been shown that certain calcite crystallographic forms can produce length-slow calcite growth in open space (Dickson, 1978). It has been suggested that length-slow calcite, due to the obtuse crystallographic forms it develops from, has a slower growth rate than length-fast calcite though this has not been accurately quantified. This study confirms other findings that length-slow calcite can develop via nucleation and growth in free space, and is not only possible via replacement reactions. Furthermore, its suggested slower growth combined with an eventual transition to more Fe incorporation into the calcite crystal, supports the idea that after the initial calcite blade formation, permeability within the fracture persists for some period of time, maintaining it as an open geothermal fluid flow pathway.

Observations from combining CL, EDS, and EBSD results reveal that calcite blades have a bidirectional growth style, with material being added quickly to the growing crystal in two directions perpendicular to the c axis (McNamara et al., 2016). This has implications for the nucleation style of bladed calcite in these geothermal fractures. Scully et al. (2020) show that geothermal calcite nucleation in fractures can be strongly controlled by the mineralogy of the fracture walls via heterogenous nucleation through special orientation relationships between calcite and quartz, and calcite and adularia. We propose that bladed calcite observed in this study nucleates independently from any wall rock control as the nucleation points of many of the studied calcite blades do not occur at the fracture wall or on other calcite crystal surfaces in the vein. This is further supported by observations made using the 3D EBSD study reported here, which confirms calcite blade central points are not in contact with the fracture wall. This observation has important implications for the nucleation processes that eventually lead to bladed calcite development in geothermal fractures.

Mineral nucleation is the phase transformation of mineral components in an aqueous solution to solid crystalline minerals, accompanied by the creation of new reactive surfaces. Mineral nuclei will form at environmental interfaces, such as fluid-rock interfaces, which provide reactive sites for heterogeneous mineral nucleation followed by growth via continuous material addition. This process is referred to as ‘classical’ nucleation theory (Burton et al., 1951; Gibbs, 1878), and has been demonstrated to be an important process in calcite precipitation (Jun et al., 2016). However, recent studies also confirmed that ‘non-classical’ nucleation is also an important process in calcite formation (Nielson et al., 2014; De Yoreo et al., 2013). ‘Non-classical’ nucleation involves the presence and action of nanoclusters within the fluid as the basic building blocks for subsequent mineral growth (Teng, 2013; Gebauer and Cölfen, 2011; Penn and Banfield, 1998). We suggest that the bladed calcite textures, and growth patterns established from combined CL, EDS, and EBSD data point towards a ‘non-classical’ calcite nucleation process occurring, involving nucleation of the calcite crystals from amorphous and/or crystalline calcite precursors within the circulating geothermal fluids. Further analysis and additional micro-nano analytical techniques will be required to confirm this theory. However, it is important to highlight this possibility, as the nucleation processes (classical and non-classical) of calcite are strongly controlled by a range of processes including interfacial energies on mineral surfaces, amount of free space for mineralisation and its effect on nucleation rates, and the composition of the solution calcite precipitates from including degree of supersaturation, salinity, and organic content (Nielson et al., 2014). As the nucleation processes are a critical aspect of how subsequent calcite crystal growth occurs, it is clear a deeper understanding is required regarding which nucleation processes occur in geothermal systems.

4.2 Timing of geothermal calcite scaling

Two main considerations need to be made when applying U-Th dating to hydrothermal vein calcite. Firstly, geothermal precipitated calcite can often entrain minute amounts of detrital material, generally in the form of silicic inclusions, during formation (Schwarcz and Latham, 1989). If enough of this detrital material is captured during the ablation process it can negatively impact the ability to perform accurate dating as it can contribute varying levels of U and Th during the ablation process (Schwarcz and Latham, 1989; Geyth, 2001). If this situation arises, not all collected U and Th amounts can be assumed to be present in the calcite from decay alone. There have been numerous studies to quantify the effectiveness of dating carbonates with extensive levels of Th from silicate inclusions or “dirty calcite” (Schwarcz and Latham, 1989; Ludwig and Titterington, 1994). Secondly, it is thought that the precipitation of bladed calcite in geothermal boiling environments can occur rapidly (Tulloch, 1982; Simmons and Christenson, 1994). This, combined with the low diffusivity of both Th and U in carbonates may suggest that calcite blades act as closed systems whose chemistry should be representative of the time it was precipitated, meaning that U-series dating can theoretically provide the precipitation date, barring the aforementioned impacts of impurities.

Measured Th/U ratios from the calcite veins in all three samples are a magnitude higher than that required for U-Series dating. This is due to an elevated Th concentration, and as a result are unsuitable for dating. In order to perform successful U-Th dating on these

veins, the source of the elevated Th needs to identified and separated from the Th generated by the decay of U. The measured Th/U ratios are >1 and as such may suggest that the vein system has not remained closed since precipitation (Sturchio and Binz, 1988). This is supported by evidence of prolonged fluid flow through this vein as evidenced by the CL zonation patterns. Another source of the elevated Th may be the ablation of minute silicate inclusions within the calcite crystals. Plotting our Th against Si data suggests this may be, at least in part, contributing to the high Th levels recorded. Analyzing Si and Ti content between ablations made at crystal edges and crystal cores reveal higher Th and Si at crystal edges, suggesting minute material trapped between calcite crystals may be contaminating the data. Earlier attempts to date geothermally precipitated calcite at Tauhara Geothermal Field also noted elevated levels of Th and the presence of silicate components (Grimes et al., 1998). Grimes et al. (1998) determined that calcite mineralization in their samples to be 99,000 ± 44,000 years old, well within the accepted 200,000-year-old lifespan of this field. Values made in this study are within the same range as those measured by Grimes et al. (1998) and so despite not being able to produce an age in this study, the technique holds promise for further investigation if appropriate corrections for the data can be determined and used (Ku and Liang, 1984; Schwarcz and Latham, 1989; Bischoff and Fitzpatrick, 1991; Ludwig and Tittering, 1994).

4.3 Insights into geothermal reservoir conditions and fluid origins

MRA and WBV analyses can be used to constrain slip systems responsible for the observed crystallographic distortion and deformation microstructures noted from EBSD on calcite (Bestmann and Prior, 2003). To do this we consider these slip systems as either screw or edge dislocations. Screw dislocations build twist boundaries with misorientation axes perpendicular to the slip plane of the dislocation system. Edge dislocations build tilt boundaries, and for minerals with trigonal symmetry (calcite) the misorientation axes lie within the slip plane, normal to the slip direction (Bestmann and Prior, 2003). In calcite it is expected that the main r and f slip systems, and the basal slip system, have MRAs perpendicular to the slip direction when only one slip system is active (de Bresser, 1991).

For the observed <2° misorientation distortions observed across calcite blades, a *c* direction MRA and an *a* or *m* direction Burgers vector fit the criteria for an edge dislocation using the *c*(0001)< $\bar{1}2\bar{1}0$> calcite slip system. In this case the calcite *c* MRA would sit within the *c* slip plane, and be normal to both <*a*> and the *m* pole. The few 2°-5° subgrain boundaries investigated in these calcite blades have an *m* pole MRA which, according to Bestmann and Prior (2003), is best explained by a basal-*a* edge dislocation i.e. *m*{$10\bar{1}0$}< $\bar{1}2\bar{1}0$>, which can facilitate the observed *c* Burgers vector, though a *c* Burgers vector is unreported in commonly observed calcite slip systems. A known slip system cannot be fit to the observed *sd* MRA and *f* Burgers vector for the 5°-10° subgrain boundaries observed in these calcite blades. Examining the blocky calcite crystals in the older fracture the MRA around an *m* pole or *a* direction has been used to infer the action of a basal-*a* edge dislocation, and the common *r*{$10\bar{1}4$}<$\bar{2}021$> or *f*{$\bar{1}012$}<$10\bar{1}1$> systems respectively (Bestmann and Prior, 2003), though again it is difficult to resolve the appearance of a *c* Burgers vector to a known slip system here. The *a* MRA for both 2°-5° and 5°-10° subgrain boundaries in the older vein blocky calcite crystals can be produced by two common calcite edge dislocation systems; *r*{$10\bar{1}4$}<$\bar{2}021$> or *f*{$\bar{1}012$}<$10\bar{1}1$>.

Various studies show that the activity of calcite slip systems can be related to the temperature under which they are operating (Bresser and Spiers, 1997; 1993). As such, combined analyses of calcite MRA and WBV to identify the activity of certain slip systems may prove a useful tool for determining temperature conditions under which calcite precipitation occurred under (by examining growth microstructure such as subtle crystal distortion), and subsequent conditions it experienced in the reservoir post precipitation (by examining deformation microstructures like subgrain boundaries). A transition from low temperature slip systems (e-twins, and *r*{$10\bar{1}4$}<$\bar{2}021$> and *f*{$\bar{1}012$}<$10\bar{1}1$>) gives way to higher temperature slip systems (*c*(0001)< $\bar{1}2\bar{1}0$>, *r*{$10\bar{1}4$}<$\bar{2}021$> or *f*{$\bar{1}012$}<$10\bar{1}1$>) at ~400°C. All low temperature systems are defined in the older fracture blocky calcite suggesting it has not been deformed at temperatures higher than 400°C since it was precipitated. The possibility of the active *c*(0001)< $\bar{1}2\bar{1}0$> in the younger bladed calcite vein however suggests this system has been at times exposed to temperatures greater than this. It is possible however that the <2° crystal distortion in bladed calcite is not the result of deformation on this slip system at higher temperatures, but that it is present in the calcite as a result of crystal growth under low levels of supersaturation (McNamara et al., 2016). Calcite growth can occur by step flow, the advancement of individual molecular layers generated at crystal imperfections (Gratz et al., 1993), or by two-dimensional surface nucleation (Dove and Hochella, 1993). Calcite crystal growth has been examined for a range of supersaturations. Teng et al. (2000) noted that when supersaturation exceeded ~0.8, calcite growth via step growth at crystal defects, dislocation, and grain boundaries, is accompanied by homogeneous surface nucleation. We suggest here that the observed *c*(0001)< $\bar{1}2\bar{1}0$> dislocation system for calcite distortion in bladed calcite vein is the result of growth under low levels of supersaturation via a step growth on crystal defect model, rather than by deformation at >400°C. This is what gives rise to the observed calcite distortion, and explains the lack of evidence for higher temperature deformation using the *c*(0001)< $\bar{1}2\bar{1}0$> slip system in the older vein blocky calcite crystals.

Chemical signatures in calcite can be used to make inferences on the nature of the fluid the calcite precipitated from. Calcite with a positive Eu anomaly may indicate that precipitating fluids acquired their REE signature during fluid-rock interaction with plagioclase-rich igneous rocks (Lee et al., 2003). Plagioclase exhibits a positive Eu anomaly due to preferential incorporation of Eu relative to REE during igneous crystallization. However, plotting calcite ΔEu/Eu against Sr wt%, another element enriched in plagioclase crystals, from bladed calcite in our samples reports a negative correlation indicating a more complex origin for the increased Eu in these calcite veins. Positive Eu anomalies have also been used to infer calcite precipitation at temperatures exceeding 200-250 °C (Bau and Möller, 1992), which fits with known fluid temperature conditions in the Kawerau Geothermal Field (Milicich et al., 2018). Conversely, negative Eu anomalies in calcite can be attributed to fluid REE compositions being derived from fluid-rock interaction with evolved, felsic igneous rocks (McLennan et al., 1990), or due to fluid undergoing reduction (Hazarika et al., 2016), thus excluding Eu from calcite during precipitation. In the case of the former cause, calcite would be expected to be enriched in a variety of incompatible elements (e.g. Rb, Nb) which is not observed, and in the case of the latter cause, calcite would be expected to preferentially incorporate Fe and Mn during crystallization. Negative trends of Eu against Fe and Mn, support this explanation, as do the CL zonation patterns observed from the bladed calcite examined in this study. Thus, we suggest that calcite reservoir scaling at Kawerau Geothermal Field, or at least part of the scaling process, occurred due to the hydrothermal fluids undergoing reduction.

CL zonation patterns in calcite are often attributed to be caused by fluctuations in bulk fluid composition (Shore and Fowler, 1996). However, other mechanisms may operate to create chemical zonation within a mineral while the precipitating solution composition remains approximately constant, such as precipitation rate, pH, supersaturation, the presence of organic material, and temperature (Nancollas and Reddy, 1971; Plummer et al., 1978; Busenberg and Plummer, 1986; Christoffersen and Christoffersen, 1990; Shiraki and Brantley, 1995). Much more investigation is needed to resolve the use of calcite chemical mapping as a tool for identifying geothermal fluid chemistries over time, and future work will also need to consider the dependence of calcite growth kinetics upon a large variety of parameters.

5. CONCLUSION

- CL, EDS, and EBSD data suggest initial growth of bladed calcite in geothermal fractures creates a skeleton framework that's acts to prop open the fluid flow pathway promoting a period of prolonged permeability.
- CL, EDS, and EBSD data reveal bladed calcite can form via 'non-classical' nucleation processes in geothermal fractures which has important considerations for scaling rates and scaling volumes in a reservoir around a borehole.
- MRA and WBV analyses prove useful tools to determine the action of various slip systems in calcite deformation, which shows potential for use as a geothermal system geothermometer.
- EBSD, CL and EDS can reveal crystal distortion patterns that relate to calcite scaling growth mechanisms controlled by fluid chemistry (e.g. supersaturation levels).
- U-Th dating of calcite scaling is possible though requires careful data acquisition and correction in order to obtain accurate ages.
- LA-ICPMS of calcite scaling can reveal important information on fluid composition but further microanalytical datasets are required in tandem to define accurately the source of various chemical signatures observed in calcite scale.

REFERENCES

Ankit, K., Urai, J.L. and Nestler, B., 2015. Microstructural evolution in bitaxial crack-seal veins: A phase-field study. Journal of Geophysical Research: Solid Earth, 120(5), pp.3096-3118.

Batzle, M.L. and Simmons, G., 1976. Microfractures in rocks from two geothermal areas. Earth and Planetary Science Letters, 30(1), pp.71-93.

Bau, M., & Möller, P. (1992). Rare earth element fractionation in metamorphogenic hydrothermal calcite, magnesite and siderite. Mineralogy and Petrology, 45(3-4), 231-246.

de Bresser, J. H. P. (1991). Intracrystalline deformation of calcite (Doctoral dissertation, Instituut voor Aardwetenschappen der Rijksuniversiteit Utrecht).

de Bresser, J. H. P., & Spiers, C. J. (1997). Strength characteristics of the r, f, and c slip systems in calcite. Tectonophysics, 272(1), 1-23.

de Bresser, J. T., & Spiers, C. J. (1993). Slip systems in calcite single crystals deformed at 300–800 C. Journal of Geophysical Research: Solid Earth, 98(B4), 6397-6409.

Bestmann, M., & Prior, D. J. (2003). Intragranular dynamic recrystallization in naturally deformed calcite marble: diffusion accommodated grain boundary sliding as a result of subgrain rotation recrystallization. Journal of Structural Geology, 25(10), 1597-1613.

Bischoff, J., Fitzpatrick, J. (1991). U-Series dating of impure carbonites: An isochron technique using total-sample dissolution, Geochimica et Cosmochimica Acta, 55, 543-554.

Bons, P.D., Elburg, M.A. and Gomez-Rivas, E., 2012. A review of the formation of tectonic veins and their microstructures. Journal of Structural Geology, 43, pp.33-62.

Brown, S.R., 1995. Simple mathematical model of a rough fracture. Journal of Geophysical Research: Solid Earth, 100(B4), pp.5941-5952.

Burton, W.K., Cabrera, N. and Frank, F.C., 1951. The growth of crystals and the equilibrium structure of their surfaces. Phil. Trans. R. Soc. Lond. A, 243(866), pp.299-358.

Busenberg, E., Plummer, L. N., & Mumpton, F. A. (1986). A comparative study of the dissolution and crystal growth kinetics of calcite and aragonite. Studies Diagenesis USGS Bull, 1578, 139-168.

Christenson, B.W., (1987). Fluid - Mineral Equilibria in the Kawerau Hydrothermal System, Taupo Volcanic Zone, New Zealand (Ph.D. Thesis) University of Auckland, New Zealand.

Christoffersen, M. R., & Christoffersen, J. (1992). Possible mechanisms for the growth of the biomaterial, calcium hydroxyapatite microcrystals. Journal of crystal growth, 121(4), 617-630.

Dickson, J. A. D. (1978). Length-slow and length-fast calcite: A tale of two elongations. Geology, 6(9), 560-561.

Dobson, P.F., Kneafsey, T.J., Hulen, J. and Simmons, A., 2003. Porosity, permeability, and fluid flow in the Yellowstone geothermal system, Wyoming. Journal of Volcanology and Geothermal Research, 123(3-4), pp.313-324.

De Yoreo, J. J.; Waychunas, G. A.; Jun, Y.-S.; Fernandez-Martinez, A. In situ Investigations of Carbonate Nucleation on Mineral and Organic Surfaces. Rev. Mineral. Geochem. 2013, 77, 229−257.

Dove, P. M., & Hochella Jr, M. F. (1993). Calcite precipitation mechanisms and inhibition by orthophosphate: In situ observations by Scanning Force Microscopy. Geochimica et cosmochimica acta, 57(3), 705-714.

Fukuda, D., Maruyama, M., Nara, Y., Hayashi, D., Ogawa, H. and Kaneko, K., 2014. Observation of fracture sealing in high-strength and ultra-low-permeability concrete by micro-focus X-ray CT and SEM/EDX. International Journal of Fracture, 188(2), pp.159-171.

Gebauer, D. and Cölfen, H., 2011. Prenucleation clusters and non-classical nucleation. Nano Today, 6(6), pp.564-584.

Genter, A., Castaing, C., Dezayes, C., Tenzer, H., Traineau, H., & Villemin, T. (1997). Comparative analysis of direct (core) and indirect (borehole imaging tools) collection of fracture data in the Hot Dry Rock Soultz reservoir (France). Journal of Geophysical Research: Solid Earth, 102(B7), 15419-15431.

Genter, A., Evans, K., Cuenot, N., Fritsch, D., Sanjuan, B., (2010). Contribution of the explora- tion of deep crystalline fractured reservoir of Soultz to the knowledge of enhanced geothermal systems (EGS). Compt. Rendus Geosci. 342, 502–516.

Geyth, M. (2001). Reflections on the 230Th/U dating of dirty material, Geochronometria, 20, 9-14.

Gibbs, J.W., 1878. On the Equilibrium of Heterogeneous Substances. American Journal of Science and Arts (1820-1879), 16(96), p.441.

Gratz, A. J., Hillner, P. E., & Hansma, P. K. (1993). Step dynamics and spiral growth on calcite. Geochimica et Cosmochimica Acta, 57(2), 491-495.

Griffiths, L, M. J. Heap, F. Wang, D. Daval, H. A. Gilg, P. Baud, J. Schmittbuhl, A. Genter. (2016). Geothermal implications for fracture-filling hydrothermal precipitation. Geothermics, 64, 235-245.

Grimes, S., Rickard, D., Hawksworth, C., Calsteren, P., Browne, P. (1998). A U-Th calcite isochron age from an active geothermal field in New Zealand, Journal of Volcanology and Geothermal Research, 81, 327-333.

Hazarika, P., Mishra, B., & Pruseth, K. L. (2016). Scheelite, apatite, calcite and tourmaline compositions from the late Archean Hutti orogenic gold deposit: Implications for analogous two stage ore fluids. Ore Geology Reviews, 72, 989-1003.

Hedenquist, J.W., Reyes, A.G., Simmons, S.F. and Taguchi, S., 1992. The thermal and geochemical structure of geothermal and epithermal systems: a framework for interpreting fluid inclusion data. European Journal of Mineralogy, pp.989-1016.

Jun, Y.S., Kim, D. and Neil, C.W., 2016. Heterogeneous nucleation and growth of nanoparticles at environmental interfaces. Accounts of chemical research, 49(9), pp.1681-1690.

Katz, J. L., Reick, M. R., Herzog, R. E., & Parsiegla, K. I. (1993). Calcite growth inhibition by iron. Langmuir, 9(5), 1423-1430.

Ku, T., Liang, Z. (1984). The dating of impure carbonates with decay series isotopes, Nuclear Instruments and Methods in Physics Research, 233(1-3), 563-571.

Lander, R.H. and Laubach, S.E., 2015. Insights into rates of fracture growth and sealing from a model for quartz cementation in fractured sandstones. Bulletin, 127(3-4), pp.516-538.

Landrot, G., Ajo-Franklin, J.B., Yang, L., Cabrini, S. and Steefel, C.I., 2012. Measurement of accessible reactive surface area in a sandstone, with application to CO2 mineralization. Chemical Geology, 318, pp.113-125.

Lee, S. G., Lee, D. H., Kim, Y., Chae, B. G., Kim, W. Y., & Woo, N. C. (2003). Rare earth elements as indicators of groundwater environment changes in a fractured rock system: evidence from fracture-filling calcite. Applied Geochemistry, 18(1), 135-143.

Limberger, J., T. Boxem, M. Pluymaekers, D. Bruhn, A. Manzella, P. Calcagno, F. Beekman, S. Cloetingh, J.-D. van Wees. (2018) Geothermal energy in deep aquifers: A global assessment of the resource base for direct heat utilization. Renewable and Sustainable Energy Reviews, 82, 961-975.

Lister, A., (2016). Analysis of Reservoir Fracture Sealing in an Active Geothermal System, Kawerau Geothermal Field, New Zealand, MSc Thesis, University of Otago, New Zealand.

Long, J. V. P., & Agrell, S. O. (1965). The cathodo-luminescence of minerals in thin section. Mineralogical Magazine and Journal of the Mineralogical Society, 34(268), 318-326.

Lu, S. M. (2018). A global review of enhanced geothermal system (EGS). Renewable and Sustainable Energy Reviews, 81, 2902-2921.

Ludwig, K., Tittering, D. (1994). Calculation of 230Th/U isochrones, ages, and errors, Geochimica et Cosmochica Acta, 58 (22), 5031-5042.

Machel, H. G. (1985). Cathodoluminescence in calcite and dolomite and its chemical interpretation. Geoscience Canada, 12(4).

McLennan, S. M., Taylor, S. R., McCulloch, M. T., & Maynard, J. B. (1990). Geochemical and Nd-Sr isotopic composition of deep-sea turbidites: crustal evolution and plate tectonic associations. Geochimica et Cosmochimica Acta, 54(7), 2015-2050.

McNamara, D. D., Massiot, C., & Milicich, S. M. (2017). Characterizing the subsurface structure and stress of New Zealand's geothermal fields using borehole images. Energy Procedia, 125, 273-282.

McNamara, D. D., Lister, A., & Prior, D. J. (2016). Calcite sealing in a fractured geothermal reservoir: Insights from combined EBSD and chemistry mapping. Journal of Volcanology and Geothermal Research, 323, 38-52.

McNamara, D.D., Faulkner, D., McCarney, E., (2014). Rock Properties of Greywacke Basement Hosting Geothermal Reservoirs, New Zealand: Preliminary Results. Proceedings, Thirty-Ninth Workshop on Geothermal Reservoir Engineering.

Melia, A., Faulkner, D.R., McNamara, D.D., (2019), Physical property characterisation of the Waipapa Greywacke: An important geothermal reservoir basement rock in New Zealand (in prep).

Meyer, H. J. (1984). The influence of impurities on the growth rate of calcite. Journal of Crystal Growth, 66(3), 639-646.

Milicich, S. D., Chambefort, I., Wilson, C. J. N., Charlier, B. L. A., & Tepley, F. J. (2018). The hydrothermal evolution of the Kawerau geothermal system, New Zealand. Journal of Volcanology and Geothermal Research, 353, 114-131.

Mountassir, G.E., Lunn, R.J., Moir, H. and MacLachlan, E., 2014. Hydrodynamic coupling in microbially mediated fracture mineralization: Formation of self-organized groundwater flow channels. Water Resources Research, 50(1), pp.1-16.

Nancollas, G. H., & Reddy, M. M. (1971). The crystallization of calcium carbonate. II. Calcite growth mechanism. Journal of colloid and interface science, 37(4), 824-830.

Nielsen, M. H.; Aloni, S.; De Yoreo, J. J. In situ TEM Imaging of CaCO3 Nucleation Reveals Coexistence of Direct and Indirect Pathways. Science 2014, 345, 1158−1162.

Penn, R.L. and Banfield, J.F., 1998. Imperfect oriented attachment: dislocation generation in defect-free nanocrystals. Science, 281(5379), pp.969-971.

Plummer, L. N., Wigley, T. M. L., & Parkhurst, D. L. (1978). The kinetics of calcite dissolution in CO 2-water systems at 5 degrees to 60 degrees C and 0.0 to 1.0 atm CO 2. American journal of science, 278(2), 179-216.

Schwarcz, H., Latham, A. (1989). Dirty calcites: 1. Uranium-series dating of contaminated calcite using leachates alone, Chemical Geology (Isotope Geosciences Section), 80, 35-43.

Scully, A., McNamara, D.D., Piazolo, S., Chambefort, I. (2020). Fracture wall crystallography control on mineral scaling in geothermal reservoirs: Preliminary results. World Geothermal Congress 2020.

Shiraki, R., & Brantley, S. L. (1995). Kinetics of near-equilibrium calcite precipitation at 100 C: An evaluation of elementary reaction-based and affinity-based rate laws. Geochimica et Cosmochimica Acta, 59(8), 1457-1471.

Shore, M., & Fowler, A. D. (1996). Oscillatory zoning in minerals; a common phenomenon. The Canadian Mineralogist, 34(6), 1111-1126.

Simmons, S., Christenson, B. (1994). Origins of calcite in a boiling geothermal system, American Journal of Science, 294, 361-400.

Sonney, R. and Mountain, B.W., 2013. Experimental simulation of greywacke–fluid interaction under geothermal conditions. Geothermics, 47, pp.27-39.

Sturchio, N., Binz, C. (1988). U-Series age determination of calcite veins, VC-1 drill core, Valles Caldera, New Mexico, Journal of Geophysical Research, 93-B6, 6097-6102.

Taron, J. and Elsworth, D., 2009. Thermal–hydrologic–mechanical–chemical processes in the evolution of engineered geothermal reservoirs. International Journal of Rock Mechanics and Mining Sciences, 46(5), pp.855-864.

Teng, H. H., Dove, P. M., & De Yoreo, J. J. (2000). Kinetics of calcite growth: surface processes and relationships to macroscopic rate laws. Geochimica et Cosmochimica Acta, 64(13), 2255-2266.

Tulloch, A. (1982). Mineralogical observations on carbonate scaling in geothermal wells at Kawerau and Broadlands, Proceedings of the 4th New Zealand Geothermal Workshop.

Urai, J.L., Williams, P.F. and Van Roermund, H.L.M., 1991. Kinematics of crystal growth in syntectonic fibrous veins. Journal of Structural Geology, 13(7), pp.823-836.

Wallis, I.C., McNamara, D.D., Rowland, J., Massiot, C., (2012). The nature of fracture permeability in the basement greywacke at Kawerau geothermal field, New Zealand. Proceedings thirty-Seventh Workshop on Geothermal Reservoir Engineering.

Wheeler, J., Mariani, E., Piazolo, S., Prior, D. J., Trimby, P., & Drury, M. R. (2009). The weighted Burgers vector: a new quantity for constraining dislocation densities and types using electron backscatter diffraction on 2D sections through crystalline materials. Journal of microscopy, 233(3), 482-494.